



Electrostatic tweezer for droplet manipulation

Yuankai Jin^{a,1}, Wanghui Xu^{a,1}, Huanhuan Zhang^a, Ruirui Li^b, Jing Sun^a, Siyan Yang^a, Minjie Liu^a, Haiyang Mao^b, and Zuankai Wang^{a,c,2}

^aDepartment of Mechanical Engineering, City University of Hong Kong, Kowloon, Hong Kong Special Administrative Region 999077, People's Republic of China; ^bInstitute of Microelectronics, Chinese Academy of Sciences, Beijing 100029, People's Republic of China; and ^cResearch Center for Nature-Inspired Engineering, City University of Hong Kong, Kowloon, Hong Kong Special Administrative Region 999077, People's Republic of China

Edited by Tom Krupenkin, University of Wisconsin–Madison, Madison, WI; received March 21, 2021; accepted November 29, 2021 by Editorial Board Member Joanna Aizenberg

Various physical tweezers for manipulating liquid droplets based on optical, electrical, magnetic, acoustic, or other external fields have emerged and revolutionized research and application in medical, biological, and environmental fields. Despite notable progress, the existing modalities for droplet control and manipulation are still limited by the extra responsive additives and relatively poor controllability in terms of droplet motion behaviors, such as distance, velocity, and direction. Herein, we report a versatile droplet electrostatic tweezer (DEST) for remotely and programmatically trapping or guiding the liquid droplets under diverse conditions, such as in open and closed spaces and on flat and tilted surfaces as well as in oil medium. DEST, leveraging on the coulomb attraction force resulting from its electrostatic induction to a droplet, could manipulate droplets of various compositions, volumes, and arrays on various substrates, offering a potential platform for a series of applications, such as high-throughput surface-enhanced Raman spectroscopy detection with single measuring time less than 20 s.

tweezer | droplet manipulation | electrostatic induction | SERS

Since the emergence of optical tweezers that are capable of trapping and manipulating microparticles in a remote and noninvasive manner in 1986 (1), the tweezers have evolved to diverse forms, such as magnetic tweezers (2) and acoustic tweezers (3). These tweezers have been widely used to manipulate many kinds of micro-/nanometal particles, bioparticles, liquid droplets, and so on. In particular, well-controlled liquid droplet manipulation is essential to various practical fields (4–7), such as printing technology (8), heat management (9–11), water harvesting (12, 13), biological assays (14), chemical reactions (15, 16), and frost prevention (17, 18). Despite remarkable significances, the droplet manipulation using these physical tweezers has achieved less progress, probably owing to the fluidic nature of droplets, which are soft and deformable in diverse operating conditions and mediums. Current approaches to manipulating droplets mainly take advantage of surface force gradient (3, 4, 9, 19–27) or the force directly applied to droplets, which always demands the responsiveness of substrates or droplets for force sources. As one of the most important physical fields to generate driving force, the electric field offers the intrinsic advantage that most types of droplets and conductive substrates (28, 29), unlike other external stimuli such as magnetism (30) or light (31, 32), respectively.

Among various electric-based manipulations, electrowetting on dielectric has been widely explored (33–35). However, these conventional electric-based droplet manipulations are deeply dependent on sophisticated electrode patterns and rational electric circuit control, which increase the complexity of manipulation platforms. Other methods eliminating the need for electrode groups, such as surface charge printing or electrostatic repulsion methods (26, 27), are susceptible to the extra steps to generate charges on substrates or droplets and therefore, are accompanied by manipulation instability due to undesirable triboelectrification during the droplet motion.

Here, we report a versatile droplet electrostatic tweezer (DEST) for remote and noninvasive manipulation of droplets on the basis of electrostatic induction. Due to the inherent responsiveness of liquid droplets to the electrostatic field, the droplets on conductive superhydrophobic surfaces obtain temporary and adjustable induced charges, and therefore, they could be trapped and guided by a noncontact tweezer, which is further proven by the diverse droplet types on diverse substrates. Such a DEST allows us to maneuver the droplets with a wide volume range (from tens of nanoliters to several milliliters) and amount range (from one to seven or more droplets) on both open surface and closed channels, even under oil. DEST could also programmatically manipulate droplets with high velocity (81.6 mm/s or faster), unlimited distance, agile direction steering, and a precise droplet stopping point without the need for any responsive agents in droplets and substrates, which offers a potential platform for the chemical reaction carrying solid cargo, surface-cleaning, and high-throughput surface-enhanced Raman spectroscopy (SERS) detection.

Results

Fig. 1A shows the schematic drawing of the DEST system, which comprises an electrode tip connecting with a power source, droplet, and substrate that is electrically grounded. Here, the superhydrophobic copper oxide substrates are used (characterized in *SI Appendix*, Fig. S1), aiming to reduce the

Significance

The manipulation of liquid droplets plays a crucial role in multidisciplinary applications. However, existing methods still face many challenges, such as short distance, low velocity, restricted operating conditions, the need for extra responsive additives in droplet, and so on. To circumvent these constraints, here we develop a droplet electrostatic tweezer to trap the liquid droplet or faithfully guide the droplet motion in a remote manner. Our method allows high flexibility and precision in manipulating droplets of different types, volumes, and numbers under different working conditions, such as in open and closed spaces and on flat and tilted surfaces as well as in oil medium, imparting various applications, such as high-throughput and high-sensitivity Raman detection.

Author contributions: Y.J. and Z.W. designed research; Y.J., W.X., H.Z., R.L., J.S., S.Y., M.L., H.M., and Z.W. performed research; Y.J., W.X., H.Z., and Z.W. analyzed data; and Y.J., W.X., and Z.W. wrote the paper.

The authors declare no competing interest.

This article is a PNAS Direct Submission. T.K. is a guest editor invited by the Editorial Board.

This open access article is distributed under [Creative Commons Attribution-NonCommercial-NoDerivatives License 4.0 \(CC BY-NC-ND\)](https://creativecommons.org/licenses/by-nc-nd/4.0/).

¹Y.J. and W.X. contributed equally to this work.

²To whom correspondence may be addressed. Email: zuanwang@cityu.edu.hk.

This article contains supporting information online at <http://www.pnas.org/lookup/suppl/doi:10.1073/pnas.2105459119/-DCSupplemental>.

Published January 6, 2022.

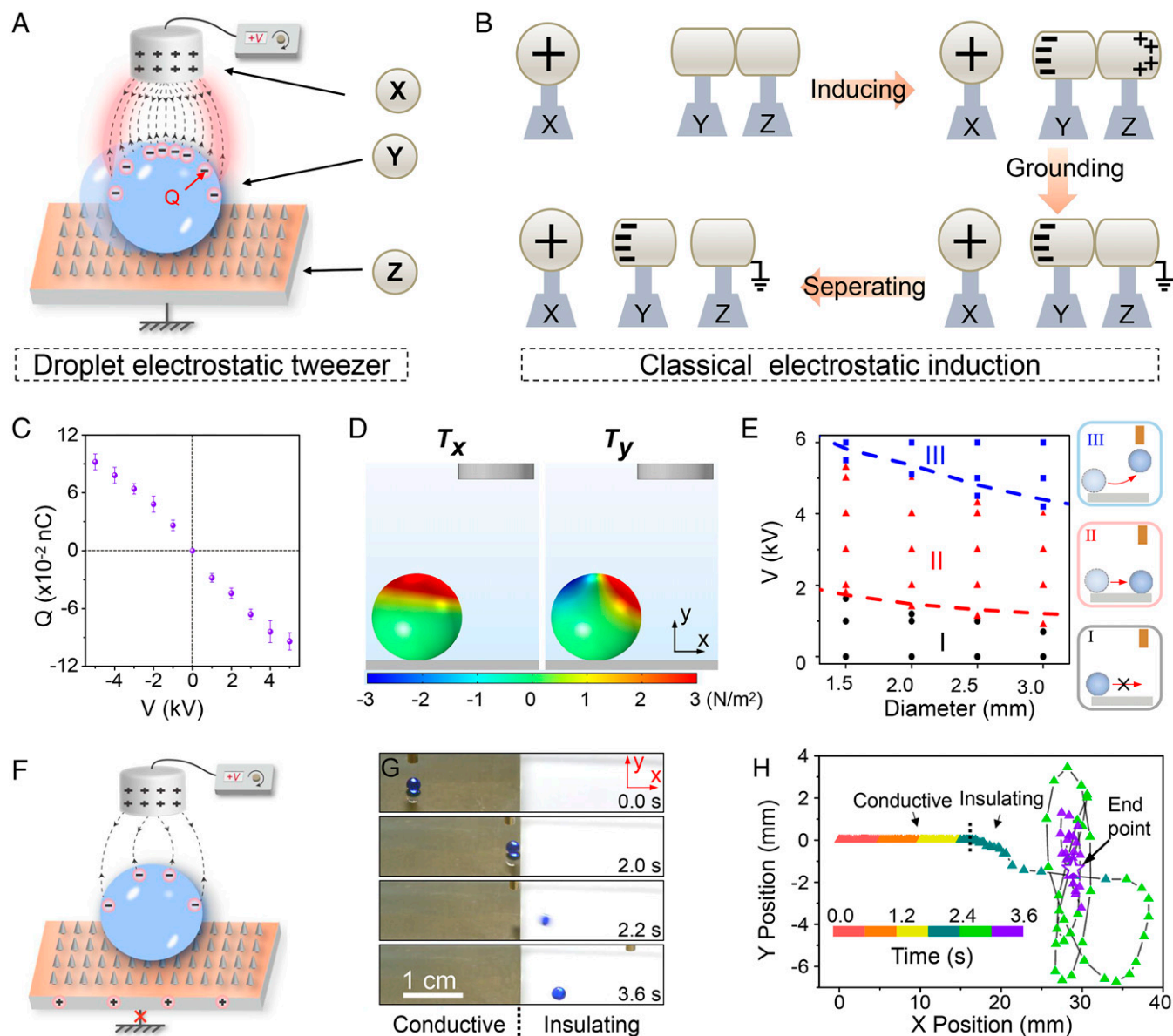


Fig. 1. Demonstration and mechanism of the DEST. (A) Schematic drawing of the DEST platform that comprises a liquid droplet on grounded substrate, and an electrode tip connecting with a power source. The Q and V denote the induced charges in droplet and applied voltage, respectively. (B) The classical schematic drawing of electrostatic induction in solid materials. The closing of charged object X electrostatically induces redistribution of charges in object Y and Z, where negative charges gather on the left side of object Y and positive charges gather on the right side of object Z. When Z is grounded, its positive charges would be neutralized by the ground. By separating Y and Z, the negative charges remain in Y, and such charges stemming from electrostatic induction are defined as induced charges. (C) The variation of induced charges in the water droplet ($\sim 7 \mu\text{L}$) as a function of the applied voltage of the tweezer with a diameter of 2 mm. The positive and negative values denote the polarity of induced charges. The error bars are based on the SD values of five tests. (D) Maxwell stress tensor exerting on the droplet in the lateral direction (T_x) and the vertical direction (T_y). These results are based on the finite-element analysis of the water droplet ($\sim 7 \mu\text{L}$) under the tweezer voltage of 4 kV, and the tweezer diameter is 2 mm. (E) Phase diagram showing different droplet dynamic behaviors under various applied voltages (V) and electrode diameters. In region I (black circles), the droplet is stationary. In region II (red triangles), the droplet moves horizontally toward the tweezer, and in region III (blue squares), the droplet finally detaches from the surface due to overlarge coulomb force. The red and blue dashed lines illustrate the minimum voltages for regions II and III, respectively, suggesting the agreement between the simulation and experimental results. (F) Schematic drawing for electrostatic induction of water droplets on nongrounded substrates. In contrast to on grounded substrates, the magnitude of induced charges in droplets on nongrounded substrates is less. (G) Time-resolved optical images showing the motion of a colored water droplet on the patterned polystyrene substrates with and without electrically conductive (gold) coating. The water droplet on the gold-coated region (conductive and being grounded) moves following the electrode (from 0.0 to 2.0 s), but the droplet on the non-coated region (insulating) is not faithful to the tweezer (from 2.2 to 3.6 s); therefore, it finally stops at a random position. (H) The x - y position of the water droplet denoting the real-time droplet position when it moves from conductive to the insulating area.

solid/liquid friction. When an external voltage is applied on the electrode tip, electrostatic induction causes the redistribution of charges in droplet and substrate, which is similar to the well-known classical electrostatic induction of conductive solid materials (Fig. 1B) (36, 37). In brief, the charged object X

electrostatically induces the redistribution of charges in objects Y and Z when they are closing (step 1), and the charges distributed in Z are then neutralized by grounding (step 2). After separating Y and Z (step 3), the charges that remain in Y could be directly measured. Accordingly, induced charges (Q) in water

droplets under the various applied tweezer voltages (V) could also be quantitatively measured by separating droplets and substrates (illustrated in *SI Appendix, Fig. S2A*), and Fig. 1C shows the linear relationship between Q and V , expressed as $Q = -0.02 V$. Such a result suggests that the induced charges in droplets can be tailored by voltages applied to the tweezer, causing the adjustable electrostatic coulomb force between tweezer and droplet (*SI Appendix, Fig. S3*). Note that the generation of induced charges in droplets is reversible in an on-demand manner (*SI Appendix, Fig. S4*). In this system, the electrode tip that provides the electrostatic induction to the droplet is reminiscent of an invisible tweezer, in analog to other physical modalities tweezers (1, 2).

The adjustable coulomb force F_C exerting on the droplet could be quantified via the following equation:

$$F_C = \oint T_{ij} \cdot n dS, \text{ with } T_{ij} = \epsilon_0 \left(E_i E_j - \frac{\delta_{ij}}{2} E^2 \right), i, j = x, y,$$

where T_e , n , ϵ_0 , δ_{ij} , and E are the Maxwell stress tensor, the surface unit normal, the permittivity of air, the Kronecker delta function, and the magnitude of the electric field intensity, respectively (38). T_{ij} in the lateral direction (T_x) and vertical direction (T_y) is obtained by finite-element analysis using the COMSOL-Multiphysics simulation, demonstrated in Fig. 1D.

Note that the F_C in the direction perpendicular to the plane is symmetric, and thus, there is no actual force on the droplet.

On the basis of adjustable electrostatic interaction between the droplet and the tweezer, we determined three different scenarios of droplet dynamic behaviors by both theoretical analysis and experimental observation (Fig. 1E and *SI Appendix, Fig. S5* and *Note S1*). In region I, the droplet remains stationary because the coulomb force is small relative to the lateral adhesion force. As the voltage increases (region II), the droplet moves horizontally and finally stabilizes at the position below the tweezer. This state is the main focus of our work, in which the voltage required for the steady droplet manipulation also depends on the diameter of tweezer (*SI Appendix, Fig. S6*). In region III, the droplet is lifted by the tweezer because of the strong electrostatic force (*SI Appendix, Fig. S7*). Note that the droplet dynamics are independent of the polarity of the applied voltages (*SI Appendix, Fig. S8*).

The well-controlled droplet manipulation in the DEST also demands that substrates should be grounded and electrically conductive to provide a free channel for charge release. The electrically conductive but nongrounded substrates could also obtain induced charges, causing the less induced charges in droplets (Fig. 1F and *SI Appendix, Fig. S9A*). As a result, the DEST's control for droplets is weaker due to the reduced electrostatic force even totally collapsed, which is detailed in

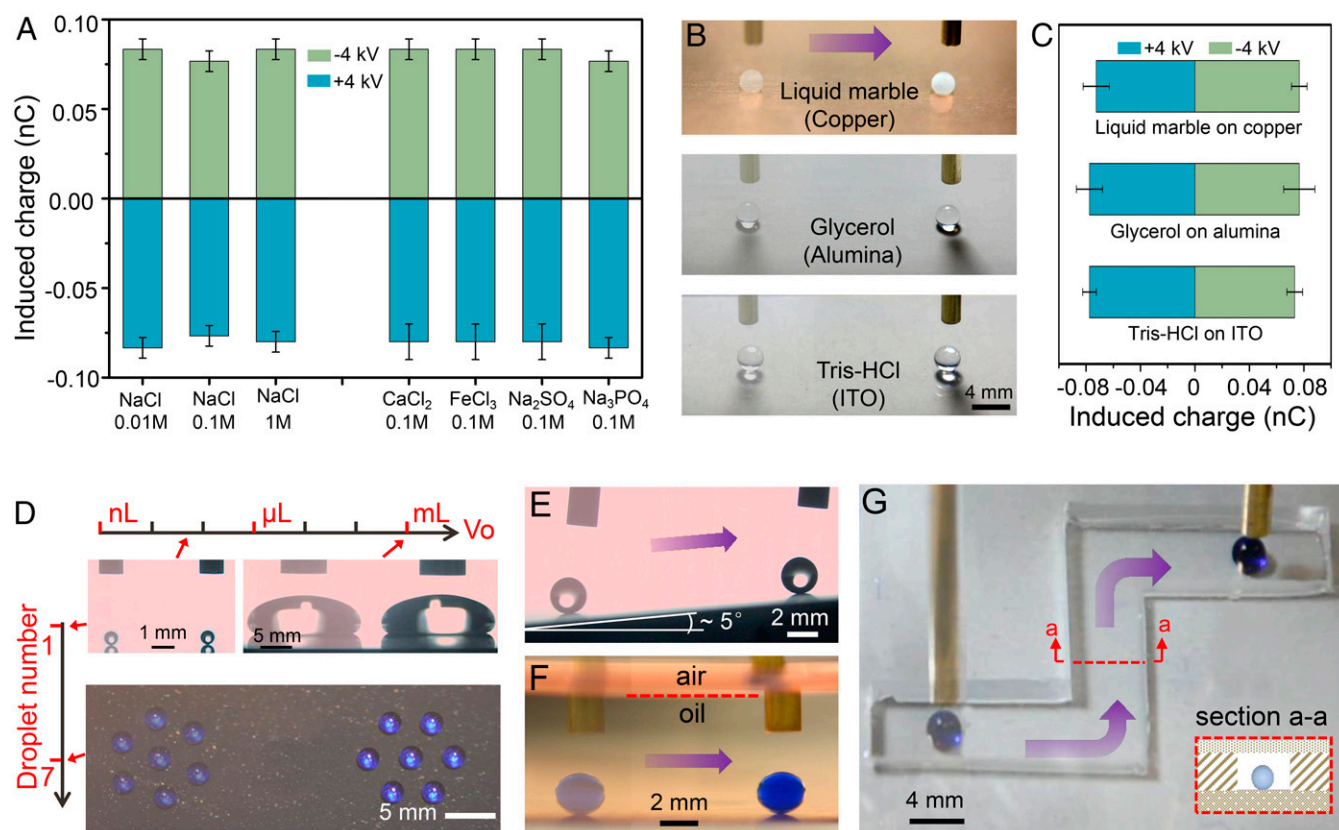


Fig. 2. The generality of the DEST for diverse types of (A–C) droplets on electrically conductive substrates, (D) droplets with various volumes and arrays, and (E–G) operating conditions. (A) The magnitude and polarity of induced charges in different salt aqueous droplets on superhydrophobic copper oxide. Regardless of salt concentration and ionic valent, the magnitudes of induced charges in droplets are almost identical. The error bars are based on the SD values of three tests. (B) The time-lapse trajectory of liquid marble on copper, glycerol on superhydrophobic alumina, and Tris-HCl on superhydrophobic ITO surface and (C) their corresponding induced charges. These three substrates are grounded. (D–G) The diverse manipulation condition for the DEST. (D) The volume range (V_0) and the number range for droplet manipulation. The time-lapse trajectory shows the manipulation of one droplet with the volume from tens of nanoliters to several milliliters as well as the manipulation of seven droplets in an array. The droplets are moved from the left toward the right, and the semitransparent images are their initial positions. Optical images show the well-controlled transport of water droplets (E) on a sloped surface with an angle of $\sim 5^\circ$, (F) under the silicon oil, and (G) in a closed channel with a zigzag track. G, Inset illustrates section a–a of the closed channel. There is a grounded copper sheet at the bottom of the oil.

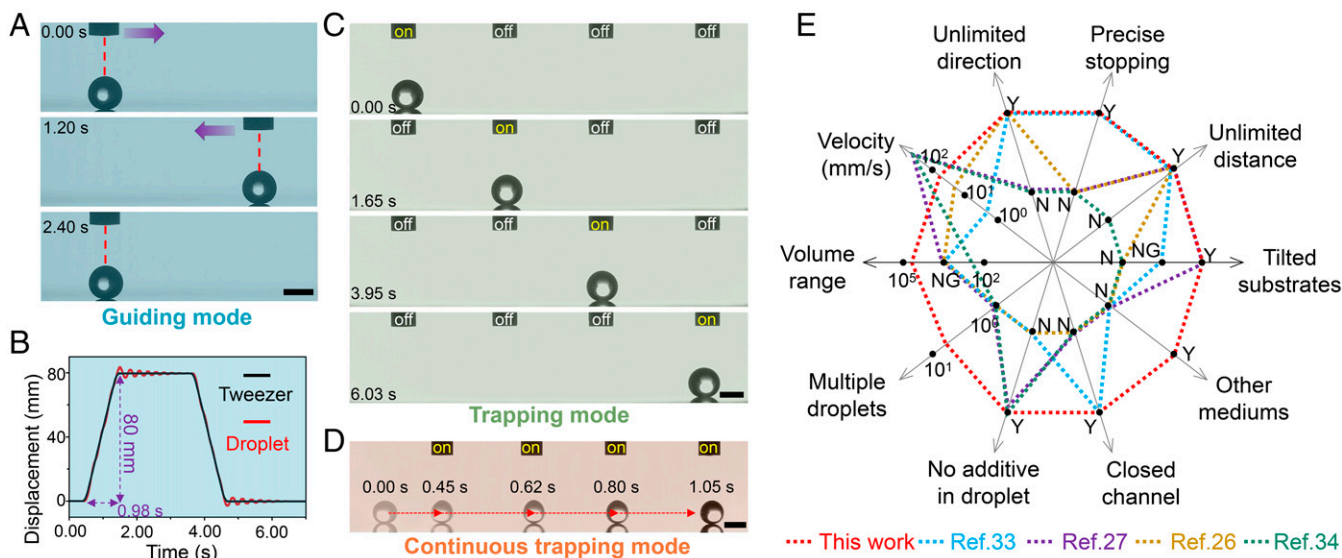


Fig. 3. Droplet manipulation modes and advantages of the DEST. (A) The guiding mode of the DEST. High-speed camera snapshots show that the droplet moves faithfully following the electrode. The colored arrows denote the moving direction of the water droplet. (B) The time-dependent displacement of a water droplet (red line) and electrode (black line) in the guiding mode. According to the displacement (80 mm) and time (0.98 s) of the droplet, its average velocity can be calculated as ~ 81.6 mm/s. (C) The trapping mode of the DEST. High-speed camera snapshots show that the water droplet moves toward the stationary tweezer with the on state. By successively changing the tweezer state, the droplet could move to any wanted position of tweezer. (D) The continuous trapping mode of the DEST. In such a mode, all tweezers are on. The time-lapse trajectory shows that the droplet continuously moves from the first tweezer to the fourth tweezer. On and off in C and D denote whether a voltage is applied to the tweezer. All of these results are based on the ~ 7 - μL water droplet moving on the superhydrophobic copper oxide surface under the control of the tweezer with voltage of 4 kV. (Scale bars: A, C, and D, 2 mm.) (E) Comparison between the DEST and previously reported electric-based droplet manipulation from 10 items. “Y,” “N,” and “NG” denote yes, no, and not given in the literature, respectively.

SI Appendix, Note S2. The importance of grounded and electrically conductive substrates is further revealed by comparing the droplet manipulation on grounded conductive substrates and insulating substrates. Briefly, we deposited a gold layer (~ 40 nm) on the left part of the insulating polystyrene surface and then sprayed a commercial superhydrophobic spray on the surface to make the whole surface superhydrophobic. When the tweezer is moved from the grounded gold-coated (conductive area) to the noncoated (insulating) area, the colored water droplet first moves following the tweezer from 0.0 to 2.0 s. However, upon moving to the insulating area, the droplet escapes from the control of the tweezer and stops at a random position at 3.6 s (Fig. 1G and Movie S1). The time-resolved x - y position of the water droplet (Fig. 1H) depicts that the droplet regularly moves on the gold-coated area but that it randomly moves on the noncoated area and finally stops at an unpredictable endpoint. Such undesired movement mainly results from the electrostatic interaction of droplets with randomly distributed triboelectric charges on the insulating surface (39) (SI Appendix, Note S3).

The DEST is generic to diverse types of droplets on electrically conductive substrates, larger or smaller droplets, droplet arrays formed by multidroplets, and various operating conditions. Given the vital roles of electrostatic induction in the DEST, we first considered the effect of the droplet’s conductivity on induced charges in droplets. By adding various concentrations (0.01, 0.1, and 1 M) of NaCl into the droplets, we obtained droplets with various conductivity (SI Appendix, Fig. S10) and measured their induced charges under the DEST. In Fig. 24, the amounts of induced charges in these droplets are almost the same under both 4- and -4 -kV tweezer voltages. In addition, Fig. 24 also demonstrates the induced charges in droplets are not affected by the salt types and their ionic valences, such as bivalent (CaCl_2 , Na_2SO_4) and trivalent (FeCl_3 , Na_3PO_4) ions. These results indicate that the magnitudes of induced charges of droplets and hence, their motion velocities are not sensitive to

the salt concentration and ion types (SI Appendix, Fig. S11). Furthermore, we also demonstrated the manipulation of liquid marble on a copper surface, glycerol on a superhydrophobic alumina surface, and tris(hydroxymethyl)aminomethane hydrogen chloride (Tris-HCl) buffer on a superhydrophobic indium tin oxide (ITO)-coated glass surface (Fig. 2B and Movie S2). In all these cases, liquids are responsive to the electric field, as affirmed by the induced charge measurement (Fig. 2C). In comparison, liquid droplets with weak responsiveness to the electric field, such as apolar and insulating silicon oil, cannot be manipulated because of minimal interaction between the tweezer and the droplet (SI Appendix, Fig. S12).

Different from previously reported methods, the remote and spatially distributed coulomb force of the DEST allows us to manipulate the droplets with a wide range of volumes and even droplet arrays (Movie S3). Fig. 2C shows that droplets with volumes ranging from tens of nanoliters to several milliliters could be moved by the tweezer, demonstrating a broad volume range up to five orders of magnitude, which is three orders of magnitude higher than that reported in recent work (40). Furthermore, the DEST could also simultaneously manipulate multidroplets in an array because the droplets carry the same polarity of electrostatically induced charges, as shown in the lower part of Fig. 2C where seven droplets are manipulated without merging. This kind of multidroplet manipulation is rarely reported in the literature to the best of our knowledge. Indeed, more droplets could also be remotely manipulated by changing the applied voltage and diameter of the tweezer, and these droplets always spontaneously form an array. In addition to on an open plane surface, the remote electrostatic force also allows us to precisely manipulate the droplet on a sloped surface (Fig. 2D), under oil environment (Fig. 2E), and in a closed channel with a zigzag track (Fig. 2F), which is shown in Movie S4. Another intriguing point of this manipulation method is that the electrode connecting with the power supply could be replaced by objects carried triboelectric charges. SI Appendix,

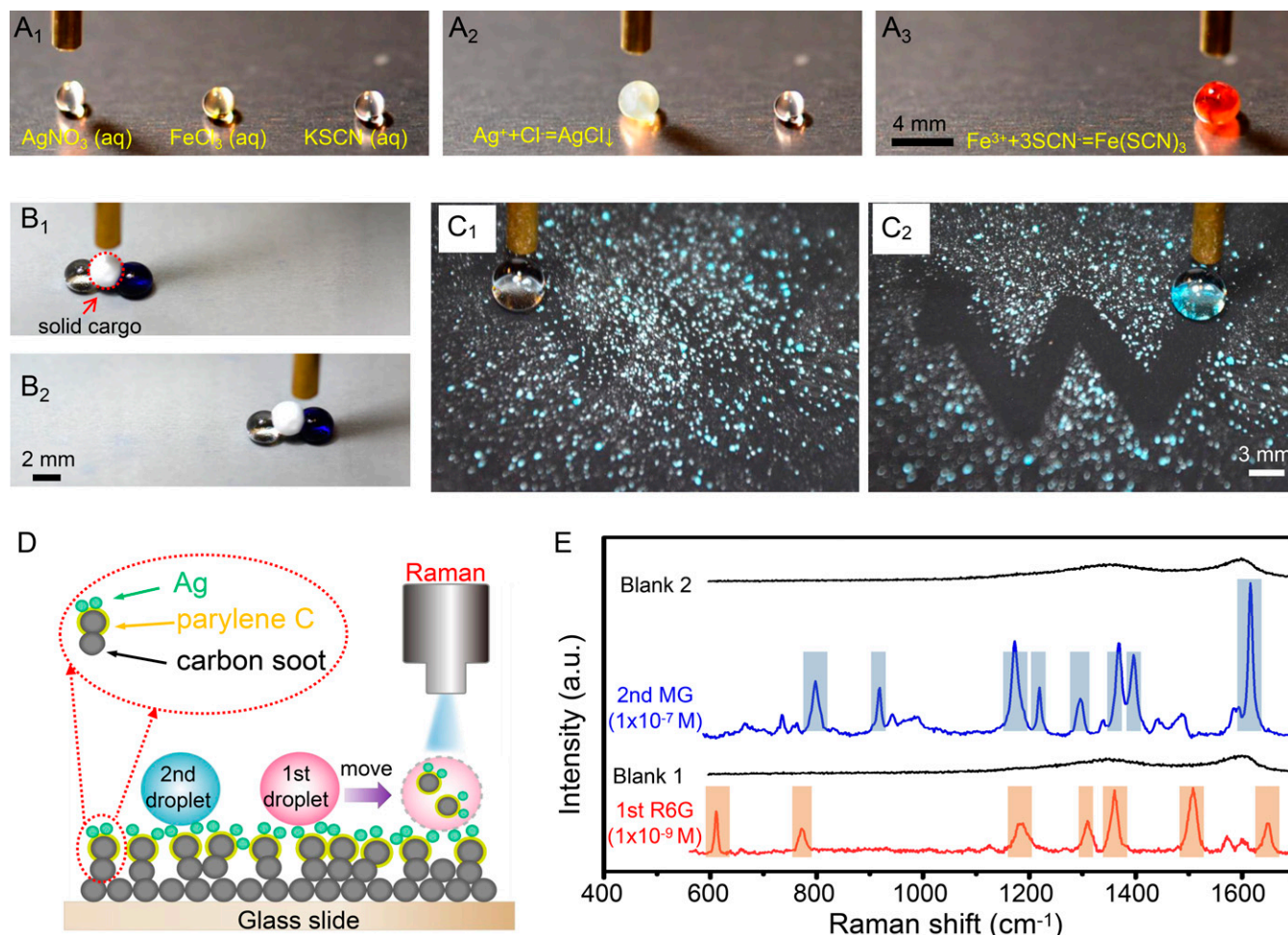


Fig. 4. The applications of the DEST. (A) Sequential images showing the electrostatic manipulation of droplets for chemical reaction. (A_1 and A_2) A 0.1 M AgNO_3 aqueous droplet is guided by the DEST to merge with the 0.1 M FeCl_3 aqueous droplet, and the coalescing droplet becomes muddy due to the formation of AgCl . (A_2 and A_3) The muddy droplet containing Fe^{3+} is further manipulated to react with the 0.05 M KSCN aqueous droplet, generating the red $\text{Fe}(\text{SCN})_3$. (B) The transportation of a solid sphere driven by two water droplets. (B_1 and B_2) The cargo carrier system moving toward the right is mainly driven by the colored water droplet. (C) Surface-cleaning application of the DEST. (C_1 and C_2) "W"-shaped track is cleaned by the droplet. (D) Schematic drawing of the DEST-based SERS platform. The superhydrophobic substrates are functionalized by successively depositing parylene C and silver nanoparticles on a carbon soot-coated glass slide. The droplet carried with analyst obtains the plasmonic silver particle during its movement to the laser point, therefore showing an enhanced sensitivity of Raman detection. After the measurement, the first droplet is moved away, and then, the second droplet is moved to the detected point by the DEST. (E) The Raman spectra of an R6G aqueous droplet (1×10^{-9} M), MG (1×10^{-7} M), and the blank substrates after removing these droplets on the same detected point. The unit for intensity, a.u., means the arbitrary unit. The colored area denotes the typical peaks of R6G and MG.

Fig. S13 shows the droplet manipulation by glass rods with positive static charges and rubber rods with negative charges, demonstrating a low-energy consumption property of such a DEST.

The distinctive features of the DEST are further revealed by different droplet manipulation modes in response to the actuation of tweezer, including the guiding mode, the trapping mode, and the continuous trapping mode. Fig. 3A shows that the droplet moves faithfully under the guidance of the tweezer, referred to as the guiding mode. Unlike other reported methods in which a predetermined pathway for droplets is required (27, 34, 35), the manifestation of the guiding mode enables the droplet to move to any desired position simply by programming the motion of the tweezer. However, at a higher average velocity (~ 81.6 mm/s) (Fig. 3B and Movie S5), the droplet still synchronously follows the motion of the tweezer, benefiting from its fast responsiveness for electrostatic induction (~ 16 ms) (SI Appendix, Fig. S14). Such spatiotemporal precision in the guiding mode is of great importance for many applications where liquid droplets are involved, such as a microreactor. In the trapping mode, a droplet moves in a manner of damping oscillation

and is finally trapped by the tweezer (SI Appendix, Fig. S15), which is analog to the trapping of nanoparticles by the optical tweezer. As shown in Fig. 3C, by sequentially activating the state of individual tweezer in an on-demand manner, a droplet can be manipulated to the preferred position (Movie S6). In contrast, in the continuous trapping mode, all tweezers are "on," and a droplet continuously moves along with the tweezer arrays (Fig. 3D and Movie S7). Taken together, our DEST demonstrates overwhelmingly collective performances over other counterparts in the aspects of droplet motion behavior, manipulating condition, and less limitation for the droplet itself (Fig. 3E).

The precise and flexible manipulation of droplets can be harnessed for many practical applications ranging from microreactor, carrying cargo, to surface cleaning (Movie S7). The reduced volume of droplets enables them to serve as promising reactors for chemical reactions, such as the precipitation reaction, the color reaction (Fig. 4A), and some charge-dominant reactions (41). In addition, the droplet could also act as a vehicle to carry cargo (Fig. 4B). In brief, a solid sphere carried by two water droplets is transported to the wanted position under the guide of

the tweezer. Furthermore, the unlimited direction in droplet manipulation allows us to clean the contaminants on the surface with any wanted route by programming the motion of the droplet. Fig. 4C shows that the “W”-shaped area is cleaned by the droplet under the guiding of the tweezer, illustrating precise control of the DEST on droplet motion.

The superhydrophobic substrates in our DEST system can also be functionalized with specific probes as amplification agents, imparting enhanced performances for chemical/biological analysis. As a demonstration, a superhydrophobic parylene C-coated carbon soot surface was first prepared, followed by depositing a thin silver layer made of silver nanoparticles for high-sensitivity and high-throughput SERS detection. On such a substrate, droplets carrying highly diluted aqueous analyte could pick the silver nanoparticles during motion (Fig. 4D), therefore showing an enhanced sensitivity in Raman measurement due to the plasmonic properties of silver nanoparticles (42). Such a method dramatically increases the detecting efficiency and sensitivity (*SI Appendix, Fig. S14*) in comparison with the traditional method, which adds plasmonic nanoparticles into the solutions of analytes, especially for the measurement of multiple analytes. In addition, DEST-based SERS eliminates the need for precise laser focusing, analyte enrichment, and substrate replacement (43–45), offering high throughput. As a result, the whole measurement process, including moving the droplet to the detecting spot, measuring, and moving the droplet away, only costs less than 20 s. Fig. 4E depicts the Raman signals of low concentration of rhodamine 6G (R6G; 1×10^{-9} M) (Fig. 4E, red line) and malachite green (MG; 1×10^{-7} M) (Fig. 4E, blue line), and two blank signals prove that there is no residual on the surface after the droplet is moved away, which demonstrates the feasibility of the DEST in high-throughput and high-detection sensitivity.

Discussion

In summary, we demonstrate that the largely neglected electrostatic charges can be harnessed as the driving force of the invisible tweezer, imparting the versatile and remote manipulation of the droplet of different types, volumes, and numbers under different working conditions, such as in the closed tortuous channel and in oil medium. We also identify the critical conditions to achieve the tweezer-like functionalities. Compared with other techniques, our method endows high flexibility and precision in droplet motion, including achieving high average velocity, long distance, and agile direction maneuverability. We envision that the technology developed by us can find a wide range of applications where droplets are involved: for example, high-throughput biological/chemical analysis.

1. A. Ashkin, J. M. Dziedzic, J. E. Bjorkholm, S. Chu, Observation of a single-beam gradient force optical trap for dielectric particles. *Opt. Lett.* **11**, 288–290 (1986).
2. A. Snezhko, I. S. Aranson, Magnetic manipulation of self-assembled colloidal asters. *Nat. Mater.* **10**, 698–703 (2011).
3. X. Ding *et al.*, On-chip manipulation of single microparticles, cells, and organisms using surface acoustic waves. *Proc. Natl. Acad. Sci. U.S.A.* **109**, 11105–11109 (2012).
4. R. Malinowski, I. P. Parkin, G. Volpe, Advances towards programmable droplet transport on solid surfaces and its applications. *Chem. Soc. Rev.* **49**, 7879–7892 (2020).
5. J. Li, J. Li, J. Sun, S. Feng, Z. Wang, Biological and engineered topological droplet rectifiers. *Adv. Mater.* **31**, e1806501 (2019).
6. W. Zhang, Q. Sun, H.-J. Butt, Z. Wang, X. Deng, Surface charges as a versatile platform for emerging applications. *Sci. Bull. (Beijing)* **65**, 1052–1054 (2020).
7. H. Li *et al.*, Spontaneous droplets gyrating via asymmetric self-splitting on heterogeneous surfaces. *Nat. Commun.* **10**, 1–6 (2019).
8. J. Wang *et al.*, Hydrogel 3D printing with the capacitor edge effect. *Sci. Adv.* **5**, eaau8769 (2019).
9. M. Liu *et al.*, Inhibiting random droplet motion on hot surfaces by engineering symmetry-breaking Janus-mushroom structure. *Adv. Mater.* **32**, e1907999 (2020).
10. R. S. Hale, V. Bahadur, Electrowetting-based microfluidic operations on rapid-manufactured devices for heat pipe applications. *J. Micromech. Microeng.* **27**, 075004 (2017).

Materials and Methods

Sample Preparation. 1H,1H,2H,2H-perfluorodecanethiol (97%; Sigma-Aldrich), perfluorooctanoic acid (95%; Sigma-Aldrich), glycerol (99.0%; Sigma-Aldrich), MG (J&K), R6G (J&K), and salts purchased from Sigma-Aldrich, including NaCl, NaClO₂, NaOH, Na₃PO₄·12H₂O, FeCl₃, KSCN, and AgNO₃, were used without further purification.

The nanograin structure of copper oxide was obtained by chemically etching the cleaned copper in a hot (96 °C) alkaline solution including NaClO₂, NaOH, Na₃PO₄·12H₂O, and deionized water (at 3.75:5:10:100 wt ratio) for 15 min. Then, the immersion of copper oxide in a 0.5 mM 1H,1H,2H,2H-perfluorooctanoic acid ethanol solution for 2 h could make the copper oxide superhydrophobic. The superhydrophobic alumina substrates were obtained by successively immersing the cleaned aluminum in a 2.5 M HCl solution for 15 min, hot water (100 °C) for 5 min, and a 0.01 M perfluorooctanoic acid aqueous solution for 1 h. To render ITO-coated glass, polystyrene, gold-coated polystyrene, and other substrates superhydrophobic, these substrates were first sprayed using a commercial superhydrophobic sprayer, Glaco (purchased from Soft99 Corporation), followed by heating at 60 °C for 5 min. The SERS surface was prepared using the combined candle soot and thin-film deposition processes (42). Briefly, a candle soot layer was first formed by placing a newly prepared glass above a burning candle flame for 15 s. Then, the candle soot-coated substrate was deposited by a thin parylene C film (~150 nm) using specialized vacuum deposition equipment (Specialty Coating Systems, Inc.) as well as a thin silver film (~30 nm) composed of nanoparticles using a vacuum sputter coating apparatus (Denton Vacuum LLC).

Instrument and Characterization. The induced charges in droplets were measured using a Faraday cup connected to a nanocoulomb meter (Monroe; Model 284) using the method shown in *SI Appendix, Fig. S2*. The nanograin morphology of CuO was observed by a scanning electron microscope (QuantaTM 450; FEG). The motion of the droplet, programmatically controlled by a stepper, was recorded by a high-speed camera (Fastcam SA4; Photron Limited) and analyzed using the software ImageJ. The gold coating on the polystyrene surface was coated with a dual-target sputtering system (Q150TS; Quorum). The electric conductivities of NaCl aqueous solution were directly measured by directly immersing the probe of the handy conductivity meter (LC-DDB-1M and CT-20; Lichen Tech.) into the solutions for 10 s. The static and dynamic contact angles of water droplets on superhydrophobic surfaces were measured by a Kruss DSA100 contact angle goniometer at ambient temperature, and the results are shown in *SI Appendix, Table S1*. Here, the dynamic contact angles (θ_a and θ_r) were measured by gradually increasing or decreasing the volume of droplets until the baseline of the droplet started to move.

Data Availability. There are no data underlying this work.

ACKNOWLEDGMENTS. We acknowledge financial support from National Natural Science Foundation of China Grant 31771083; Research Grants Council of Hong Kong Grants C1018-17G, 11275216, and 11218417; Shenzhen Science and Technology Innovation Council Grant JCYJ20170413141208098; and City University of Hong Kong Grants 9680212 and 9610375. We also appreciate the help of Dr. Dangyuan Lei and Dr. Siqi Li from City University of Hong Kong and Dr. Jiaqian Li from The University of Hong Kong.

11. W. Li *et al.*, Supercapillary architecture-activated two-phase boundary layer structures for highly stable and efficient flow boiling heat transfer. *Adv. Mater.* **32**, e1905117 (2020).
12. Y. Zheng *et al.*, Directional water collection on wetted spider silk. *Nature* **463**, 640–643 (2010).
13. I. Oh *et al.*, Enhanced condensation on liquid-infused nanoporous surfaces by vibration-assisted droplet sweeping. *ACS Nano* **14**, 13367–13379 (2020).
14. I. Barbulovic-Nad, H. Yang, P. S. Park, A. R. Wheeler, Digital microfluidics for cell-based assays. *Lab Chip* **8**, 519–526 (2008).
15. A. C. Sun *et al.*, A droplet microfluidic platform for high-throughput photochemical reaction discovery. *Nat. Commun.* **11**, 1–6 (2020).
16. H. Li *et al.*, Droplet precise self-splitting on patterned adhesive surfaces for simultaneous multidetection. *Angew. Chem. Int. Ed. Engl.* **59**, 10535–10539 (2020).
17. R. Mukherjee, S. F. Ahmadi, H. Zhang, R. Qiao, J. B. Boreyko, Electrostatic jumping of frost. *ACS Nano* **15**, 4669–4677 (2021).
18. J. B. Boreyko, C. P. Collier, Delayed frost growth on jumping-drop superhydrophobic surfaces. *ACS Nano* **7**, 1618–1627 (2013).
19. A. Shastry, M. J. Case, K. F. Böhringer, Directing droplets using microstructured surfaces. *Langmuir* **22**, 6161–6167 (2006).
20. M. K. Chaudhury, G. M. Whitesides, How to make water run uphill. *Science* **256**, 1539–1541 (1992).

21. J. A. Lv *et al.*, Photocontrol of fluid slugs in liquid crystal polymer microactuators. *Nature* **537**, 179–184 (2016).
22. H. Geng *et al.*, Sunlight-driven water transport via a reconfigurable pump. *Angew. Chem. Int. Ed. Engl.* **57**, 15435–15440 (2018).
23. W. Li, X. Tang, L. Wang, Photopyroelectric microfluidics. *Sci Adv.* **6**, eabc1693 (2020).
24. J. Vialletto *et al.*, Magnetic actuation of drops and liquid marbles using a deformable paramagnetic liquid substrate. *Angew. Chem. Int. Ed. Engl.* **56**, 16565–16570 (2017).
25. J. Guo *et al.*, Omni-liquid droplet manipulation platform. *Adv. Mater. Interfaces* **6**, 1900653 (2019).
26. H. Dai *et al.*, Controllable high-speed electrostatic manipulation of water droplets on a superhydrophobic surface. *Adv. Mater.* **31**, e1905449 (2019).
27. Q. Sun *et al.*, Surface charge printing for programmed droplet transport. *Nat. Mater.* **18**, 936–941 (2019).
28. D. R. Link *et al.*, Electric control of droplets in microfluidic devices. *Angew. Chem. Int. Ed. Engl.* **45**, 2556–2560 (2006).
29. H. Mertaniemi *et al.*, Superhydrophobic tracks for low-friction, guided transport of water droplets. *Adv. Mater.* **23**, 2911–2914 (2011).
30. A. Li *et al.*, Programmable droplet manipulation by a magnetic-actuated robot. *Sci. Adv.* **6**, eaay5808 (2020).
31. Y. Zhao *et al.*, Bioinspired multifunctional Janus particles for droplet manipulation. *J. Am. Chem. Soc.* **135**, 54–57 (2013).
32. Y. Xiao *et al.*, Moving droplets in 3D using light. *Adv. Mater.* **30**, e1801821 (2018).
33. J. Li, N. S. Ha, T. Liu, R. M. van Dam, C. J. Kim, Ionic-surfactant-mediated electro-dewetting for digital microfluidics. *Nature* **572**, 507–510 (2019).
34. J. Nie *et al.*, Self-powered microfluidic transport system based on triboelectric nanogenerator and electro-wetting technique. *ACS Nano* **12**, 1491–1499 (2018).
35. L. Zheng *et al.*, Self-powered electrostatic actuation systems for manipulating the movement of both microfluid and solid objects by using triboelectric nanogenerator. *Adv. Funct. Mater.* **27**, 1606408 (2017).
36. Encyclopedia Britannica Inc., "Electric polarization" in *Encyclopædia Britannica Online* (Britannica, 2004). <https://www.britannica.com/science/electric-polarization>. Accessed 30 December 2021.
37. C. Heinert, R. M. Sankaran, D. J. Lacks, Electrostatic charge generation on material surfaces from the evaporation of liquids. *J. Electrostat.* **105**, 103450 (2020).
38. J. Berthier, *Micro-Drops and Digital Microfluidics* (William Andrew, 2012).
39. A. Z. Stetten, D. S. Golovko, S. A. L. Weber, H. J. Butt, Slide electrification: Charging of surfaces by moving water drops. *Soft Matter* **15**, 8667–8679 (2019).
40. D. Wu *et al.*, High-performance unidirectional manipulation of microdroplets by horizontal vibration on Femtosecond laser-induced slant microwall arrays. *Adv. Mater.* **32**, e2005039 (2020).
41. J. K. Lee, D. Samanta, H. G. Nam, R. N. Zare, Micrometer-sized water droplets induce spontaneous reduction. *J. Am. Chem. Soc.* **141**, 10585–10589 (2019).
42. R. Li *et al.*, Self-concentrated surface-enhanced Raman scattering-active droplet sensor with three-dimensional hot spots for highly sensitive molecular detection in complex liquid environments. *ACS Sens.* **5**, 3420–3431 (2020).
43. H. Li *et al.*, Bioinspired micropatterned superhydrophilic Au-areoles for surface-enhanced Raman scattering (SERS) trace detection. *Adv. Funct. Mater.* **28**, 1800448 (2018).
44. F. De Angelis *et al.*, Breaking the diffusion limit with super-hydrophobic delivery of molecules to plasmonic nanofocusing SERS structures. *Nat. Photonics* **5**, 682–687 (2011).
45. S. Shin *et al.*, A droplet-based high-throughput SERS platform on a droplet-guiding-track-engraved superhydrophobic substrate. *Small* **13**, 1602865 (2017).